Gamma-rays and Neutrinos from Cosmic Accelerators

Contents

1 Topics

- High energy gamma-ray emission from galactic and extragalctic sources
- Galactic sources of high energy neutrinos

1.1 ICRANet participants

- Aharonian Felix
- Sahakyan Narek

1.2 Students

- Zargaryan David
- Baghmanyan Vardan
- Karlica Mile
- Gasparyan Sargis

1.3 Ongoing collaborations

- Francesco Vissani (INFN, Gran Sasso Theory Group, Italy)
- Frank Rieger (Max-Planck-Institut für Kernphysik, Germany)
- Rui-zhi Yang (Key Laboratory of Dark Matter and Space Astronomy, China)
- Marco Tavani (INAF-IASF Roma and Universit di Roma "Tor Vergata", Italy)

- Paolo Giommi (ASI Science Data Center)
- Ulisses Barres de Almeida (Centro Brasileiro de Pesquisas Fisicas - CBPF/MCT)
- Giovanni Piano (INAF-IASF Roma, INFN Roma and Univ. Tor Vergata, Italy)

2 Brief description

The works done and currently being developed within our group lie in the field of particle astrophysics including high energy gamma and neutrino astrophysics. The detection of these particles gives the opportunity to understand the physical processes that occur in astrophysical sources: they are not affected by interaction with extragalactic and galactic electromagnetic fields before they reach the Earth, and therefore point directly to the source of emission.
Below we present several abstracts from the papers published in 2015.

- On the gamma-ray emission from 3C 120

We report the analysis of Fermi Large Area Telescope data from five years of observations of the broad line radio galaxy 3C 120. The accumulation of larger data set results in the detection of high-energy γ-rays up to 10 GeV, with a detection significance of about 8.7σ. A power-law spectrum with a photon index of 2.72 ± 0.1 and integrated flux of $F_\gamma = (2.35 \pm 0.5) \times 10^{-8}$ photon $\mathrm{cm}^{-2} s^{-1}$ above 100 MeV well describe the data averaged over five year observations. The variability analysis of the light curve with 180-, and 365- day bins reveals flux increase (nearly twice from its average level) during the last year of observation. During this period the short time interval of source detectability (7- days) indicates the compactness of the emitting region. The γ-ray spectrum can be described as synchrotron self-Compton (SSC) emission from the electron population producing the radio-to-X-ray emission in the jet. The required electron energy density exceeds the one of magnetic field only by a factor of 10 meaning no significant deviation from equipartition.

- Detection of Persistent Gamma-Ray Emission Toward SS433/W50

The microquasar SS433 features the most energetic jets known in our Galaxy. A large fraction of the jet kinetic power is delivered to the surrounding W50 nebula at the jet termination shock, from which high-energy emission and

cosmic-ray production have been anticipated. Here we report on the detection of a persistent gamma-ray signal obtained with the *Fermi* Large Area Telescope from an unidentified source which we tentatively associate, given its 99.9 % confidence level position accuracy and the lack of any other high-energy emitter counterpart in the studied region, with SS433. The obtained spectral energy distribution displays a distinct maximum at $\sim$ 250 MeV and extends only up to $\sim$ 800 MeV. We discuss the possibility that the observed gamma-ray emission is produced through proton-proton collisions at the SS433/W50 interaction regions. If the same mechanism is operating in other baryon-loaded microquasar jets, their collective contribution could represent a significant fraction of the total galactic cosmic-ray flux at GeV energies.

- Fermi-LAT observations of the Sagittarius B complex

We use 5 years of *Fermi* data towards the Galactic-centre giant molecular cloud complex, Sagittarius B, to test questions of how well-mixed the Galactic component of cosmic rays are and what the level of the cosmic-ray sea in different parts of the Galaxy is. We use dust-opacity maps from the Planck satellite to obtain independent methods for background subtraction and an estimate for the mass of the region. We then present high-quality spectra of γ-ray emission from 0.3 to 30 GeV and obtain an estimate of the cosmic-ray spectrum from the region. We obtain an estimate of the mass of the region of $1.5 \pm 0.2 \times 10^7$ $M_\odot$ using the Planck data, which agrees well with molecular-line-derived estimates for the same region. We find the the γ-ray flux from this region is fitted well with a cosmic-ray spectrum that is the same as is observed locally, with evidence of a small over-density at intermediate (1–10 GeV) energies. We conclude that the γ-ray and cosmic-ray spectrum in the region can be well-fitted using a local cosmic-ray spectrum.

3 Publications-2015

- Kelner, S., Prosekin, A. and Aharonian, F. "Synchro-Curvature Radiation of Charged Particles in the Strong Curved Magnetic Fields", The Astronomical Journal, Volume 149, Issue 1, article id. 33, 21 pp., 2015.

- Bordas, P., Yang, R., Kafexhiu, E. and Aharonian, F. "Detection of Persistent Gamma-Ray Emission Toward SS433/W50", The Astrophysical Journal Letters, Volume 807, Issue 1, article id. L8, 5 pp., 2015.

- Yang, Rui-zhi, Jones, D. and Aharonian, F. "Fermi-LAT observations of the Sagittarius B complex", Astronomy & Astrophysics, Volume 580, id.A90, 7 pp. 2015.

- Sahakyan, N., Zargaryan, D. and Baghmanyan, V. "On the gamma-ray emission from 3C 120", Astronomy & Astrophysics, Volume 574, id.A88, 5 pp., 2015.

- Sahakyan, N., Yang, R., Rieger, F., Aharonian, F. and de Ona-Wilhelmi, E. "High Energy Gamma Rays from Centaurus a" Proceedings of the MG13 Meeting on General Relativity ISBN 9789814623995, pp. 1028-1030, 2015.

3.1 Publications-2010-2014

- Sahakyan, N., Piano, G. and Tavani, M. "Hadronic Gamma-Ray and Neutrino Emission from Cygnus X-3", The Astrophysical Journal, Volume 780, Issue 1, article id. 29, 2014.

- Sahakyan, N., Rieger, F., Aharonian, F., Yang, R., and de Ona-Wilhelmi, E. "On the gamma-ray emission from the core and radio lobes of the radio galaxy Centaurus A", International Journal of Modern Physics: Conference Series, Volume 28, id. 1460182, 2014.

- Sahakyan, N., Yang, R. Aharonian, F. and Rieger, F., " Evidence for a Second Component in the High-energy Core Emission from Centaurus A?", The Astrophysical Journal Letters, Volume 770, Issue 1, L6, 2013.
- Yang, R.-Z., Sahakyan, N., de Ona Wilhelmi, E., Aharonian, F. and Rieger, F., "Deep observation of the giant radio lobes of Centaurus A with the Fermi Large Area Telescope", Astronomy & Astrophysics, 542, A19, 2012.
- Sahakyan, N., "High energy gamma-radiation from the core of radio galaxy Centaurus A", Astrophysics, 55, 14, 2012.
- Sahakyan, N., "On the Origin of High Energy Gamma-Rays from Giant Radio Lobes Centarus A", International Journal of Modern Physics Conference Series, 12, 224, 2012.
- Vissani, F., Aharonian, F. and Sahakyan, N.,"On the detectability of high-energy galactic neutrino sources", Astroparticle Physics, 34, 778, 2011.

4 On the gamma-ray emission from 3C 120

4.1 Introduction

The γ-ray detection by Fermi Large Area Telescope (*Fermi*) from non blazar active galactic nuclei (e.g., Cen A, [6]; M87, [1]; NGC 1275, [2]) shows that these are different and potentially very interesting classes of γ-ray emitters. This provides an alternative approach for studying high energy emission processes compared to blazars where the emission is strongly Doppler boosted.
At the red shift $z = 0.033$, 3C 120 is a nearby Seyfert 1 radio galaxy that is an active and powerful emitter of radiation at all the observed wavebands. With bright continuum and broad optical emission lines 3C 120 is usually classified as a broad line radio galaxy (BLRG). Hosting a black hole with a mass $5.5 \times 10^7 M_\odot$, well constrained from the reverberation mapping [45], 3C 120 has a radio morphology more similar to the Fanaroff-Riley class I radio sources [20]. The source has a powerful one-sided radio jet extending from a sub-*pc* up to 100 *kpc* scales [56]. Observations with the Very Long Baseline Array at frequencies (22, 43, and 86 GHz) reveal a very rich inner jet structure containing several superluminal components with apparent speed up to 4-6 *c* [32, 26, 25] that can be investigated with better resolution than most other extragalactic superluminal sources because of the relatively low redshift. The jet inclination angle to the line of sight is constrained to be 14° by the measured apparent motion [19]. Recently, using X-ray and radio observations, [41] found that dips in the X-ray emission are followed by ejections of bright superluminal knots in the radio jet, which clearly establishes an accretion-disk-jet connection.
In X-rays, 3C 120 is a bright ($\approx 5 \times 10^{-11}$ erg cm^{-2}s^{-1} at 2-10 keV) and variable source on time scales from days to months [27]. The *ASCA* observation shows a broad iron line K_α that can be fitted by Gaussian with $\sigma = 0.8$ keV and equivalent width of 400 eV. The knots in the jet of 3C 120 observed in ra-

dio and optical bands have also been detected later in the X-ray band with the *ROSAT* and *Chandra* [30], which indicates the existence of high energy non-thermal particles in these knots. The origin of X-ray emission is highly debated especially when the extrapolation of synchrotron emission fails to take this emission into account. In these cases it can be explained by the inverse-Compton scattering of cosmic microwave background (CMB) photons or by proton synchrotron emission; If so, this component can be extended up to MeV/TeV range [58, 8].
At high energies (HE; > 100 MeV) the source was not detected with the energetic gamma-ray experiment telescope on board the Compton Gamma Ray Observatory, despite several pointing observations [38]. The 2σ upper limit on the source flux above 100 MeV was set to $9 \times 10^{-8}\,\mathrm{cm}^{-2}\,\mathrm{s}^{-1}$. Afterward, the source was detected with the *Fermi* using 15 months of all-sky exposures [5]. The averaged HE spectrum between 100 MeV and 1 GeV can be described by the power law with photon index $\Gamma = 2.71 \pm 0.35$ and an integral flux $F(E > 100\,\mathrm{MeV}) = (2.9 \pm 1.7_{\mathrm{stat}}) \times 10^{-8}\,\mathrm{cm}^{-2}\,\mathrm{s}^{-1}$ with the detection significance of 5.6σ. However the source is not included in the *Fermi* second source catalog ([43], 2FGL) since the averaged signal appeared to be below the required 5σ threshold. This might be evidence of the long-term variability of the flux, since for a steady γ-ray signal the accumulation of longer data set (24 versus 15 months) should result in an increase of the detection significance $\approx \sqrt{24/15} \times 5.6\sigma$.
[5] and [36] investigated the temporal variations of the γ-ray flux (above 100 MeV) over short timescales. The light curve binned in three-month-long periods shows only a few episodes when the flux increased on a level more than 3σ. One such episode occurred during the 15-month data set [5] and two occurred during the 24-month data set [36]. The rest of the time, the source was undetectable by *Fermi* . This was interpreted as a GeV flux variation on 90-day scales. However considering only two periods out of eight have been detected and taking trials into account, post-trial significance probably is even lower than 3σ. Therefore, these conclusions were inconclusive considering the limited statistics of the detected signal.
The peculiar structure of 3C 120 implies different sites (sources) as the origin of the detected GeV γ-rays . Clearly, analogous with blazars, the non thermal beamed radiation can be produced in the innermost part of the jet on scales less than a kilo-parsec (but not strongly boosted because of the larger jet inclination angle compared to blazars). In fact, a powerful jet observed at an inclination angle $\theta \leq 14^{\circ}$, producing radio to x-ray flux (with

the luminosity $\sim 10^{45}$ erg s^{-1}) via synchrotron emission can produce Doppler boosted γ-ray flux via inverse Compton scattering. This sort of emission would appear as variable on week timescales or shorter with the luminosity $L_\gamma \sim U_{rad}/U_B\, L_{syn}$, which in principle can be detected by *Fermi* , depending on the magnetic field and emitting region size. On the other hand, the non-variable γ-ray emission from the extended structures (e.g., extended lobes, large scale jet, and knots) can extend up to the GeV energies and contribute (at least at some level) the total observed γ-ray flux. For example, a γ-ray emission from the extended lobes of nearby Centaurus A radio galaxy contributes greater than one-half of the total source emission [3, 57]. Moreover, steady γ-ray emission from 3C 120 on the level of *Fermi* sensitivity has already been predicted from the jet knots within both proton synchrotron [8] and beamed CMB inverse Compton scenarios [58]. Therefore the compact and extended structures both remain possible sites for production of the observed γ-rays .
In general the absence of statistically significant indication of variability introduces uncertainties to distinguish between different emission mechanisms. In particular for 3C 120 , given the presence of many prominent sites for γ-ray production, the possible variability (or nonvariability) is crucial for understanding the origin of HE emission. Moreover, the spectrum only extends only up to 1 GeV that does not provide any possibility to distinguish between the mechanisms using the predicted different spectral shapes. Now the larger data set allows us to study the spectrum with better statistics above 1 GeV, and to investigate the variability in detail. This motivated us to have a new look at the γ-ray emission based on the five years of *Fermi* data.
The paper is structured as follows. The results of spectral analysis are presented in Sect. 5.2. The temporal analysis is presented in Sect. 5.3. Implications of different emission mechanisms are discussed in the Sect. 5.4, and conclusions are presented in the Sect. 4.5.

4.2 Fermi-LAT data analysis

4.2.1 Data extraction

Fermi on board the Fermi satellite is a pair-conversion telescope, operating since August 4, 2008, and is designed to detect HE γ-rays in the energy range 20 MeV - 300 GeV [13]. It constantly scans the entire sky every three hours

and by default is always in the survey mode. Details about the LAT instrument can be found in [13].
For the present analysis, we use publicly available *Fermi* $\sim$ 5.3 yr data from 4th August 2008 to 4th December 2013 (MET 239557417–407808003). We use the Pass 7 data and analyze them using the Fermi Science Tools v9r33p0 software package. We select events with zenith angle $< 100^{\circ}$ and with energy between 100 MeV and 100 GeV. We only used the data when the rocking angle of the satellite was $< 52^{\circ}$, to reduce the contamination from the Earth limb γ-rays, which are produced by cosmic rays interacting with the atmosphere. We downloaded photons from a 10° region centered on VLBI radio position of 3C 120 (RA,dec)= (68.296, 5.354) and worked with a $14^{\circ} \times 14^{\circ}$ square region of interest (ROI). We bin photons with *gtbin* tool with a stereographic projection into pixels of $0.1^{\circ} \times 0.1^{\circ}$ and into 30 equal logarithmically-spaced energy bins. Then with the help of *gtlike* tool, we perform a standard binned maximum likelihood analysis. The fitting model includes diffuse emission components and γ-ray sources within ROI (the model file is created based on 2FGL) and since 3C 120 is not included in 2FGL, we added a pointlike source on the known location of 3C 120 (RA,dec)= (68.296, 5.354), [40]. The Galactic background component is modeled using the LAT standard diffuse background model *gll_iem_v05_rev1* and *iso_source_v05* for the isotropic γ-ray background. The normalization of background models as well as fluxes and spectral indices of sources within 10° are left as free parameters in the analysis.

4.2.2 Spectral analysis

We assume that the γ-ray emission from 3C 120 is described by the power law and normalization and power law index are considered free parameters, then the binned likelihood analysis is performed. From a binned *gtlike* analysis, the best-fit power law parameters for 3C 120 are

$$\left(\frac{dN}{dE}\right)_P = (4.06 \pm 1.0) \times 10^{-10} \left(\frac{E}{100\ \mathrm{MeV}}\right)^{-2.72\pm0.1} . \tag{4.2.1}$$

This corresponds to an integral flux of

$$F_\gamma = (2.35 \pm 0.5) \times 10^{-8}\ \mathrm{photon\ cm^{-2} s^{-1}}, \tag{4.2.2}$$

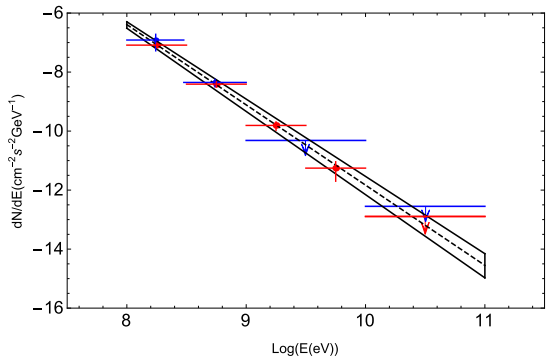

Figure 4.1: The averaged differential spectrum of 3C 120 (above 100 MeV) red points as compared with that based on the initial 15 month data set [5]. The dashed black line shows the power law function determined from the *gtlike*.

with only statistical errors taken into account. The test statistic (defined as TS = 2(log L - log L_0), where L and L_0 are the likelihoods when the source is included or not) is TS = 76.3 above 100 MeV, corresponding to a $\approx 8.7\,\sigma$ detection significance. The results are consistent with the parameters found in [5], namely photon index $\Gamma = 2.71 \pm 0.35$ and integral flux $(2.9 \pm 1.7) \times 10^{-8}$ ph cm^{-2}s^{-1} above 100 MeV. The value TS = 76.3 is above the threshold value TS=25 and 3C 120 should be included in the upcoming *Fermi* source catalogs. Figure 5.1 shows the spectrum of 3C 120 obtained by separately running *gtlike* for 5 energy bands, where the dashed line shows the best-fit power law function for the data given in Eq. (5.2.1). In comparison, results from the previous study of 3C 120 [5] are presented as blue data points. The highest energy bin (10-100 GeV), is shown as an upper limit.
Since we used the exposure almost 2.5 times longer than in 2 FGL, this can result in additional faint sources in the data that are not properly accounted for in the model file. In order to check if any additional sources were present, the *gttsmap* tool is used with the best-fit model of 0.1- 100 GeV events to create a TS significance map of the $6^\circ \times 6^\circ$ region. Nevertheless, no significant excess hot spots (TS$>$ 25) are found. Therefore, the model file used in the analysis gives a good representation of the data. Next, we obtained the source localization with *gtfindsrc*, yielding R.A. = 68.205, decl. = 5.38 with a 95% confidence error circle radius of $r_{95} = 0.05$. These localizations are offset by 0.09° from the VLBI radio position of 3C 120 (R.A. = 68.296, decl. = 5.354) [40].

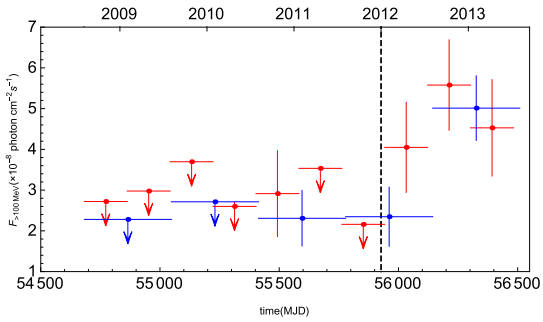

Figure 4.2: Gamma-ray light curve from August 4th 2008 to December 4th 2013. The bin size corresponds to 180- (red) and 365- days (blue). The galactic and extragalactic background emission is fixed to the best-fit parameters obtained for the overall time fit.

4.3 Temporal variability

The variability of the observed γ-ray flux could provide important constraints on the emitting region(s). The timescale of the observed flux variation τ would limit the (intrinsic) size of the γ-ray production region to $R'/\delta \leq \frac{c\tau}{1+z}$ where δ is the Doppler factor and z is the red shift. During the previous variability study, using the accumulation of 90- day *Fermi* all-sky survey exposures, the source shows two time intervals when $TS > 10$ whereas it was mostly being undetectable by *Fermi* . This could be interpreted as a possible variability at GeV energies [36].

More observational data set (increased photon statistics) can provide more detail in this regard. Accordingly, the total observational time (from August 4th, 2008 to December 4th, 2013) is divided into different timescales and light curves are generated using the unbinned likelihood analysis with *gtlike*. To minimize uncertainties in the flux estimation, the photon indices of all sources are fixed to the values obtained in 100 MeV-100 GeV energy range for the whole time period. Instead, the normalization of 3C 120 and background point sources are treated as free parameters. Since no variability is expected from the underlying background diffuse emission, the normalization of both background components is fixed to the values that were obtained for the whole time period.

Fig. 5.2 illustrates the γ-ray flux variation above 100 MeV for 180- and 365-days sampling with red and blue data points, respectively. It is noticeable that

up to $\approx$ 55400 MJD, γ-rays from 3C 120 are below *Fermi* sensitivity (detection significance TS$<$ 10). Afterward a cycle with faint γ-ray emission changes and then the produced flux is sufficient to be detected by *Fermi* . For example, the averaged flux in a year sampling is more than twice higher than its average level (see Fig. 5.2) with highest test statistics corresponding to $TS = 63.8$ (similar to 180- day sampling $TS = 38.92$). This is probably caused by the changes in emission states, e.g., the source moves in a state that is characterized by more effective production of γ-rays resulting a flux increase. This flux increase gives proof of flux variability on month timescales.
In addition to reported month timescale variability, flux variation for shorter time periods e.g., a month or sub-month time-scales has been performed over the time interval where the increase of flux was detected. Accordingly, the unibinned likelihood analysis is performed using shorter time sampling (7 - and 15 - days) for the time period $>$ 56000 MJD. A γ-ray signal from the source is detected above threshold $TS > 10$ using a sampling of only seven days. The required condition was fulfilled only in three time intervals with the maximum detection significance 4.8σ reached in the last week of September 2013. The corresponding flux is $(2.15 \pm 0.6) \times 10^{-7}$photon cm$^{-2}s^{-1}$ nearly an order of magnitude higher than average flux level presented in Eq. 5.2.2. Because of limited statistics, however, no definite conclusions about shorter time scale variability can be drawn.

4.4 Disscusion and interpretation

The monthly timescale variability of 3C 120 ($t_{var} \sim 6$ month) denotes the compactness of the emitting region. Under any reasonable assumption for Doppler boosting, $\delta = 3 - 5$, the emitting region cannot be larger than $R < \delta\, c\, t_{var} \sim 10^{18}\,(\delta/4)$ cm. This immediately allows us to exclude jet knots as the main sites where the observed γ-rays are produced. Most likely, the γ-rays are produced in a compact region of the jet, e.g., the blob moving with relativistic velocities. Generally, the broad band spectrum of blazars, as well as those from radio galaxies, which have jets oriented at systematically larger angles to our line of sight, are successfully described by the Synchrotron/Synchrotron self-Compton (SSC) model [23, 16, 14]. In this modeling the low energy emission (radio through optical) is represented as a synchrotron emission from leptons in the homogeneous, randomly oriented magnetic field (B) while the HE component (from x-ray to HE γ-ray) is an

Table 4.1: SSC modeling parameters presented in Figure 4.3. The Doppler boosting is assumed to be $\delta = 4$ and emitting region radius $R_b \sim 10^{18}$ cm.

	B(mG)	α	γ_{min}	γ_c	U_e/U_B
solid line	30	2.4	700	1.7×10^4	1.9
dashed line	25	2.8	800	9.8×10^3	16
dot dashed line	25	2.0	2500	1.2×10^4	1.3

inverse Compton scattering of the same synchrotron photons. This kind of interpretation for 3C 120 is the first choice considering the results of the modeling of the other *Fermi* observed radio galaxies [6, 1, 2]. Here we apply the SSC mechanism to model the overall SED of 3C 120 , particularly in the 0.1-100 GeV energy range. The multifrequency data (sub MeV/GeV energies) are from the simultaneous (quasi-simultaneous) observations of the 3C 120 [24].

We suppose that the emission is coming from a spherical region with the radius R_b moving with Lorentz factor $\Gamma = (1-\beta)^{-1/2}$. The emission is boosted by $\delta = 1/[\Gamma(1-\beta\cos(\theta))]$ where θ is the angle between the bulk velocity and the line of sight. The electron distribution follows $N(\gamma) \propto \gamma^{-\alpha} Exp[-\gamma/\gamma_c]$ with $\gamma > \gamma_{min}$ naturally expected from the shock acceleration theories and the electron energy density (U_e) scales with the one of the magnetic fields (U_B). Then, several independent parameters used in the modeling can be constrained from the observations. In particular, the superluminal speed puts an upper limit to the jet's inclination angle at 14° [19]. Thus, the flux would be modestly boosted with the Doppler factor $\delta = 4$ if the emitting region moves with the bulk Lorentz factor $\Gamma = 8$ at the inclination angle of 12.5°. Next, the monthly timescale variability (180− days) implies that the emitting region is confined to a volume whose radius is determined from the relation $R_b/\delta < 4.6 \times 10^{17}$ cm. The Doppler factor of $\delta \sim (3-4)$ requires an emitting region of $\sim 10^{18}$ cm.

We assume that HE emission has a pure SSC origin. As a first step, the radio data are included in the modeling, which means that the same electron population is responsible for both synchrotron and inverse-Compton emissions. The best guess values of electron energy distribution, which allows us to properly reproduce the low and HE data, corresponds to $\alpha = 2.8$, $\gamma_{min} = 800$, and $\gamma_c = 9.8 \times 10^3$ (dashed line in Fig. 4.3). Other model parame-

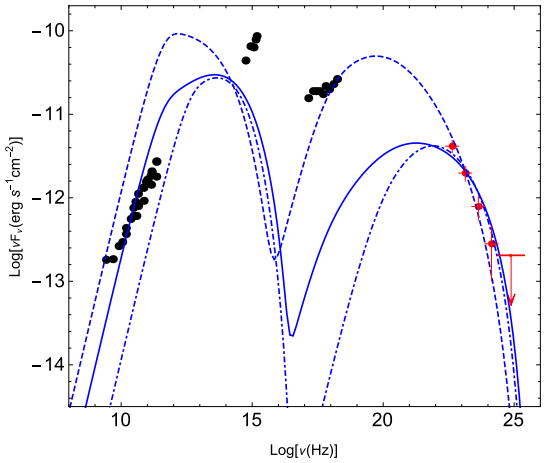

Figure 4.3: The SED of 3C 120 modeled with one-zone SSC component. Black points refers to the simultaneous (quasi-simultaneous) data from [24] and red points from *Fermi* data analysis. The solid, dashed, and dot dashed lines corresponds to $\alpha = 2.4, 2.8$, and 2, respectively. The SSC emission is calculated using a simulator developed by Andrea Tramacere [55, 54, 42] available at $http://www.isdc.unige.ch/sedtool/$.

ters are presented in Table 4.1. The ratio of nonthermal electron and magnetic field energy densities is equal to $U_e/U_B \approx 16$ (for magnetic field $B = 25$ mG). In this case, the jet power in the form of the magnetic field and electron kinetic energy, given by $L_B = \pi c R_b^2 \Gamma^2 U_B$ and $L_e = \pi c R_b^2 \Gamma^2 U_e$, respectively, are $L_B = 1.49 \times 10^{44}\,\mathrm{erg\,s^{-1}}$ and $L_e = 2.42 \times 10^{45}\,\mathrm{erg\,s^{-1}}$. The total jet power L_{jet}, defined as $L_{jet} = L_B + L_e$, corresponds to $L_{jet} \approx 2.57 \times 10^{45}\,\mathrm{erg\,s^{-1}}$, which is noticeable high. This interpretation is unlikely since the necessary jet power is of the same order as Eddington accretion power $L_{Edd} = 6.8 \times 10^{45}\mathrm{erg\,s^{-1}}$ for the $5.5 \times 10^7 M_\odot$ black hole mass in 3C 120 . This is not a strong argument considering that some blazars might operate in the super-Eddington regime as follows from observations [15].
However, this is not the case since the jet power can be relaxed, assuming the hard X-ray emission originates from the thermal Comptonization near the disk. Thus, the predicted flux from the SSC component falls below the hard X-ray limit in Fig. 4.3 (solid line). Indeed, a reasonable modeling of both radio and HE data gives an electron distribution with the index $\alpha = 2.4$ between $\gamma_{min} = 700$ and $\gamma_{cut} = 1.7 \times 10^4$. The jet energy carried out by par-

ticles (electrons) and magnetic field corresponds to $L_j = 6.27 \times 10^{44} \mathrm{erg\,s^{-1}}$, which is still high but not dramatic. Moreover, unlike the other case, the electron nonthermal and magnetic field energy densities are close to equipartition $U_e/U_B \approx 2$ (for $B = 30$ mG). Even though the ratio $U_e/U_B \approx 16$ cannot be rejected, recalling other blazars where the jet is massively out of equipartition, the later modeling has an advantage considering the required total jet power.
In principle, the radio to X-ray and γ-ray emissions can be produced in different sites (blobs). Supposing the radio flux does not exceed that presented in [24], the electron distribution with a typical power law index $\alpha = 2$ predicted from strong shock acceleration theories can reproduce HE γ-ray data (dot dashed line in Fig. 4.3). The modeling requires a relatively high low energy cutoff, $\gamma_{min} = 2500$, and energy equipartition between nonthermal electrons and the magnetic field $U_e/U_B = 1.3$ (for $B = 25$ mG). Moreover, the total jet kinetic power is $L_{jet} \approx 3.4 \times 10^{44}\,\mathrm{erg\,s^{-1}}$ approximately half that in the previous modeling. From the point of view of the necessary lower energy, this model has an advantage over previous model. Nevertheless, this modeling is very sensitive to the choice of the γ_{min}, which can be constrained only with simultaneous data. Although the radio data presented in Fig. 4.3 are not synchronous, they can be treated as an upper limit. Consequently, the expected luminosity should not be higher than the above obtained value.
In Fig. 4.3, SSC mechanism provides a good fit to all data except those in the optical/UV band $(10^{15} - 10^{16})$ Hz. This UV excess is likely caused by direct thermal emission from the accretion disk. Indeed, a thermal component with a blackbody temperature > 15000 K and a luminosity $\geq 2 \times 10^{44}\,\mathrm{erg\,s^{-1}}$ can explain detected UV flux. This lower limit to the temperature and luminosity corresponds to minimal UV flux reported in [24] and presented in Fig. 4.3, but a hotter and luminous disk is expected to explain observed data. Thus, SSC radiation plus thermal component (contribution of the accretion disk) can satisfactorily reproduce the entire SED (including UV data). However detailed modeling of the thermal component goes beyond the scope of this paper.

4.5 Conclusion

We report on the recent observations of 3C 120 with *Fermi* . The source is detected up to 10 GeV with statistically significant 8.7σ significance as

a result of the accumulation of data from a longer all-sky exposure. The photon index corresponds to $\Gamma = 2.7$, which is similar to the nearby FR1 class radio source Centaurus A with a comparable black hole mass [6] and $F_\gamma = (2.35 \pm 0.5) \times 10^{-8}$ photon cm$^{-2}s^{-1}$ photon flux above 100 MeV. Adapting the $d_L = 139.3$ Mpc distance, this equals $L_\gamma = 2.1 \times 10^{43}$erg s^{-1}, which lies in the typical isotropic γ-ray luminosity range of FR I sources detected by *Fermi* [5]. Albeit, the observed γ-ray flux is relatively faint compared with other *Fermi* detected radio galaxies ($\approx 10^{-7}$photon cm$^{-2}s^{-1}$), the isotropic γ-ray luminosity is quite impressive when compared with the Eddington luminosity $L_{Edd} = 6.8 \times 10^{45}$erg s^{-1} .

We also report an interesting modification of the γ-ray flux in time. Initially, the source described by the γ-ray flux mostly below than the *Fermi* sensitivity threshold appears to be frequently detected afterward. The flux is almost twice more than its average level in the last year of the selected time period (from 2008 to late 2013, see Fig. 5.2). This increase of flux shows monthly timescale variability of 3C 120 , indicating that the γ-rays are produced in sup-parsec regions. A common behavior of the light curves in any day sampling (a month or more) is that the source is mostly undetectable by *Fermi* prior to March 2012 then it becomes mostly γ-ray production duty cycles. Moreover, the long lasting source activity that probably continues after December 2013 (nearly two years) indicates a change in the γ-ray production state (from low to high) rather than flaring activity as seen in many blazars (generally in short timescales). In principle this change can have different physical origins. First, the change in the central engine, where possible jets obtain much of their energy from the infall of matter into a supermassive black hole, can at least have some influence. The change in the jet power, hence higher intensity γ-ray , is expected in the case when the additional matter is fueling the accretion disk. In theory, the observations of the region closer to the black hole with sensitive X-ray instruments (e.g., *Chandra*, *XMM-Newton*) can prove such a possibility. On the other hand, the environmental influence on the changes in γ-ray emission states cannot be rejected considering the large scale powerful jet up to 100 *kpc* (e.g., target interacting with the jet). Any of the above mentioned possibilities would be supported by multi-wavelength observations. This is beyond the scope of this paper and will be investigated in the future works.

One zone SSC model is used to fit broadband emission from 3C 120 . Assuming γ-rays are produced in a compact region ($\sim 10^{18}$ cm), this modeling

gives an adequate fit to the SED with modest Doppler boosting $\delta \sim 4$ and no significant bias from equipartition $U_e/U_B \approx 2$. The necessary jet kinetic power is $\approx 6 \times 10^{44}$ erg s^{-1}, which corresponds to 10 % of Eddington power.

5 On the gamma-ray emission from the core and radio lobes of the radio galaxy Centaurus A

5.1 Introduction

The bright, nearby radio galaxy Cen A is the best-studied extragalactic objects over a wide range of frequencies [34]. Its unique proximity (d$\sim$3.7 Mpc) and peculiar morphology allow a detailed investigation of the non-thermal acceleration and radiation processes occurring in its active nucleus and its relativistic outflows.
At MeV energies, Cen A has been observed with both OSSE (0.05-4 MeV) and COMPTEL (0.75-30 MeV) onboard the Compton Gamma-Ray Observatory (CGRO) in the period 1991-1995 [52]. An agreement of the OSSE spectrum with the COMPTEL one in the transition region around 1 MeV, and correlated variability has been found [52]. At higher energies, a marginal (3σ) detection of gamma-rays from the core of Cen A was reported with EGRET (0.1-1.0 GeV), but due its large angular resolution the association with the core remained rather uncertain [31]. Unlike the initial variability (month-type?) seen at lower energies, the flux detected by EGRET appeared stable during the whole period of CGRO observation [50]. At high-energy (HE; 200 MeV$<$ E $<$ 100 GeV) Fermi-LAT has recently detected γ-ray emission from the core (i.e., within $\sim 0.1^{\circ}$) and the giant radio lobes of Cen A ([4, 7]): An analysis of the available ten-month data set reveals a point-like emission region coincident with the position of the radio core of Cen A, and two large extended emission regions detected with a significance of 5 and 8σ for the northern and the southern lobe, respectively. The HE emission from the core extends up to $\sim$ 10 GeV and is well described by a power-law function with photon index $\sim$ 2.7. At VHE ($>$ 100 GeV) energies, Cen A has also been detected (with a significance of 5σ) by the H.E.S.S. array based on observations

in 2004-2008. The results show an average VHE spectrum compatible with a power law of photon index $\Gamma = 2.73 \pm 0.45_{stat} \pm 0.2_{syst}$ and an integral flux $F(E > 250\,\mathrm{GeV}) = (1.56 \pm 0.67_{\mathrm{stat}}) \times 10^{-12}\,\mathrm{cm}^{-2}\,\mathrm{s}^{-1}$[9]. No evidence for variability has been found in the H.E.S.S. data set, but given the weak signal no certain conclusions can be drawn.
i) In the case of the core the apparent lack of significant variability features at GeV and TeV energies has so far precluded robust inferences as to the physical origin of the core emission in Cen A. Unfortunately, the resolutions of current gamma-ray instruments is not sufficient to localize the gamma-ray emitting region(s) either: The angular resolutions of both the H.E.S.S. array ($\sim 0.1^\circ$) and *Fermi* (0.1° -1°, depending on energy) correspond to linear sizes of the gamma-ray emitting region(s) of about 5 kpc or larger. This $\sim$ 5-kpc-region contains several potential gamma-ray emitting sites such as the central black hole, the sub-pc- or the kpc-scale jet etc. Based on the reported results, one thus cannot distinguish whether the gamma-rays observed from the core in Cen A originate in compact or extended regions. This motivated us to have a new look on the core emission based on four year of *Fermi* data.
ii) If the extended HE emission from Cen A is generated by indeed inverse-Compton up-scattering of CMB and EBL (extragalactic background light) photons, this could offer a unique possibility to spatially map the underlying relativistic electron distribution in this source. The detection of GeV γ-rays from the radio lobes implies magnetic field strengths $\lesssim 1\ \mu$G (e.g., [4]). This estimate can be obtained quite straightforwardly from the comparison of radio and γ-rays, assuming that these radiation components are produced in the same region by the same population of electrons through synchrotron and inverse-Compton processes. In general, however, the radio and the γ-ray region do not need to coincide. While the radio luminosity depends on the product of the relativistic electron density N_e and the magnetic-field square B^2, the inverse-Compton γ-ray luminosity only depends on N_e. This implies that γ-rays can give us model-independent information about both the energy and the spatial distribution of electrons, while the radio image of synchrotron radiation strongly depends on the magnetic field. As a consequence, the γ-ray image can be larger than the radio image if the magnetic field drops at the periphery of the region occupied by electrons. This provides one of the motivations for a deeper study of the extended HE (lobe) emission region in Cen A. We analyze 3 yr of Fermi LAT data, increasing the available observation time by more than a factor of three with respect to the previously

reported results. The larger data set allows a detailed investigation of the spectrum and morphology of the lobes with better statistics, especially above 1 GeV, where the spectral shape may reflect cooling effects and/or maximum energy constraints on the parent population of particles generating the HE γ-ray emission.

5.2 The core of Cen A

For the study of HE emission from the core of Cen A we use publicly available *Fermi* $\sim$ 4 yr data from 4th August 2008 to 1st October 2012 (MET 239557417–370742403). *Fermi* on board the Fermi satellite is a pair-conversion telescope designed to detect high-energy γ-rays in the energy range 20 MeV - 300 GeV [13]. It constantly scans the entire sky every three hours and is always in survey mode although in the past some dedicated pointing observation were done. We use the Pass 7 data and analyze them using the Fermi Science Tools v9r27p1 software package. The entire data set was filtered with *gtselect* and *gtmktime* tools and retained only events belonging to the class 2, as is recommended by the Fermi/LAT science team[1]. To reject atmospheric gamma-rays from the Earth's limb, events with zenith angle $<$ 100 deg are selected. The standard binned maximum likelihood analysis is performed using events in the energy range 0.1–100 GeV extracted from a 10° region centered on the location of Cen A, which is referred to as 'region of interest' (ROI). The fitting model includes diffuse emission components and gamma-ray sources within ROI which are not associated with Cen A (the model file is created based on *Fermi* second catalog [43] and the fluxes and spectral indices are left as free parameters in the analysis. In the model file, the giant radio lobes were modeled using templates from WMAP-k band observation of the source which is extracted from NASA's SkyView. The background was parameterized with the files gal_2yearp7v6_v0.fits and iso_p7v6source.txt and the normalizations of both components were allowed to vary freely during the spectral point fitting.

[1] http://fermi.gsfc.nasa.gov/ssc/data/analysis/documentation/Cicerone/Cicerone_Data_Exploration/Data_preparation.html

5.2.1 Spectral Analysis

Initially the continuum gamma-ray emission of the core of Cen A is modeled with a single power law. The normalization and power-law index are considered as free parameters then the binned likelihood analysis is performed. From a binned *gtlike* analysis, the best-fit power-law parameters for the core of Cen A are

$$\left(\frac{dN}{dE}\right)_P = (2.73 \pm 0.12) \times 10^{-9} \left(\frac{E}{100\ \mathrm{MeV}}\right)^{-2.69\pm0.03} . \tag{5.2.1}$$

This corresponds to an integral flux of

$$F_\gamma = (1.61 \pm 0.06) \times 10^{-7}\,\mathrm{photon\,cm^{-2}}s^{-1}, \tag{5.2.2}$$

with only statistical errors taken into account. The test statistic (defined as TS = 2(log L - log L_0), where L and L_0 are the likelihoods when the source is included or not) is TS = 1978 above 100 MeV, corresponding to a $\approx 44\,\sigma$ detection significance. The results are consistent with the parameters found in [7], namely photon index $\Gamma = 2.67 \pm 0.08$ (between 200 MeV and 30 GeV) and integral flux $(1.50 \pm 0.37) \times 10^{-7}$ ph cm^{-2}s^{-1} above 100 MeV (model B). Figure 5.1 shows the spectrum of the core of Cen A obtained by separately running *gtlike* for 12 energy bands, where the dashed line shows the best-fit power-law function for the data given in Eq. (5.2.1). For the highest energy bin (56.2-100 GeV), an upper limit is shown. The spectrum shows a tendency for a deviation from a single power-law model with respect to the data above several GeV. Indeed, a χ^2 fit of the power-law model to the data gives a relatively poor fit with $\chi^2 = 39.7$ for 9 degrees of freedom (dof), and its probability is $P(\chi^2) < 2 \times 10^{-5}$. In order to investigate this in more detail, the core spectrum is modeled with a broken power-law model and *gtlike* tool is retried. The best-fit broken power-law parameters are

$$\left(\frac{dN}{dE}\right)_{BP} = (1.19 \pm 0.08) \times 10^{-13} \left(\frac{E}{E_b}\right)^{-\Gamma_{1,2}}, \tag{5.2.3}$$

and

$$F_\gamma = (1.67 \pm 0.06) \times 10^{-7}\,\mathrm{photon\,cm^{-2}}s^{-1}, \tag{5.2.4}$$

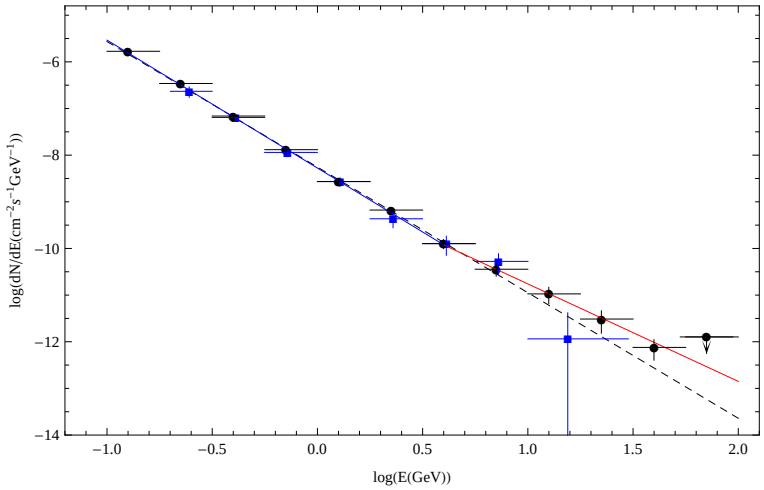

Figure 5.1: Average high-energy gamma-ray (>100 MeV) spectrum of the core of Cen A (black points - this work) as compared to the one based on the initial 10 month data set [blue squares - 7]. The dashed black line shows the power-law function determined from the gtlike. The blue and the red line show power-law fits to the energy bands below and above $E_b \simeq 4$ GeV, respectively.

with $\Gamma_1 = 2.74 \pm 0.02$ and $\Gamma_2 = 2.12 \pm 0.14$ below and above $E_b = (4.00 \pm 0.09)$ GeV, respectively. In order to compare the power-law and the broken-power-law model, a log likelihood ratio test between the models is applied. The test statistic is twice the difference in these log-likelihoods, which gives 9 for this case. Note that the probability distribution of the test statistic can be approximated by a χ^2 distribution with 2 dof, corresponding to different degrees of freedom between the two functions. The results give $P(\chi^2) = 0.011$, which again indicates a deviation from a simple power-law function. The results of the data analysis with a broken power-law model reveal a hardening of the (average) gamma-ray core spectrum towards higher energies. The "unusual" break at 4 GeV could most naturally be explained by a superposition of different spectral components. In order to study this deeper, we divide the data set into two parts, i.e., (0.1- 4) GeV and (4-100) GeV. (Note that the 4 GeV-value is obtained from binned maximum likelihood analyses). The core spectrum of Cen A in both energy ranges is then modeled with a power-law function and the *gtlike* tool is separately applied to these two energy bands. The photon index and flux between 100 MeV and 4 GeV are

$\Gamma_1 = 2.74 \pm 0.02$ and $F_\gamma = (1.68 \pm 0.04) \times 10^{-7}$ photon cm^{-2}s^{-1}, respectively, and the test statistics gives TS=1944. The result is shown with a blue line in Figure 5.1. On the other hand, for the energy range (4-100) GeV we obtain $\Gamma_2 = 2.09 \pm 0.2$ and $F_\gamma = (4.20 \pm 0.64) \times 10^{-10}$ photon cm^{-2}s^{-1}, respectively, and a TS value of 124.4, corresponding to a $\approx 11\,\sigma$ detection significance. This component is depicted with a red line in Figure 5.1. Moreover, to derive the most likely coordinates of the observed gamma-ray emission *gtfindsrc* tool is applied, yielding RA = 201.387°, Dec = −43.028° with a 95% confidence error circle radius of $r_{95} = 0.04°$and RA = 201.387°, Dec = −43.028° with $r_{95} = 0.04°$for energy ranges (0.1- 4) GeV and (4-100) GeV, respectively. This coordinates are offset by 0.04°and 0.018°from the VLBI radio position of Cen A (RA =201.365°, Dec = −43.019° [39]).

5.3 Temporal Variability

Variability, if present, could provide important constraints on the emitting region(s). An observed HE flux variation on time scale $t_{\rm var}$, for example, would limit the (intrinsic) size of the gamma-ray production region to $R' \leq \frac{\delta_D}{1+z} c t_{\rm var}$ where δ_D is Doppler factor and z is the red-shift. However, previous HE and VHE gamma-ray observations of the core of Cen A with *Fermi* [7] and H.E.S.S. [9] did not find evidence for significant variability. Here we investigate whether the longer (4 yr) data set employed changes this situation. We thus divide the whole data set (from August 4th 2008 to October 1st 2012) into different time bins and generate light curves using the unbinned likelihood analysis with *gtlike*. Due to limited photon statistics the shortest time scale that one can probe is 15 days. In our analysis we generate light curves in 15, 30, 45 and 60 day bins. The normalization of the core and background point sources are treated as free parameters, but the photon indices of all sources and the normalization of the lobes are fixed to the values obtained in 100 MeV-100 GeV energy range for the whole time period. Since no variability is expected for the underlying background diffuse emission, the normalization of both background components is fixed to the values obtained for the whole time period. To search for variability, a χ^2 test was performed. The result for the light curve with 15 day bins is $\chi^2/d.o.f. = 1.22$ and the probability is $P(\chi^2) = 0.07$. For the light curves with 30 day and 60 day bins we find $\chi^2/d.o.f. = 1.37$ and $\chi^2/d.o.f. = 1.32$, corresponding to $P(\chi^2) = 0.04$ and $P(\chi^2) = 0.127$, respectively. These results are consistent with no variability.

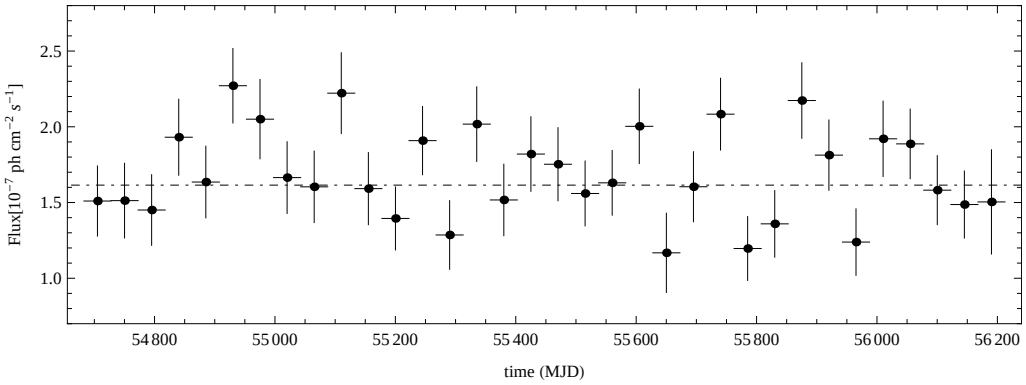

Figure 5.2: Gamma-ray light curve from August 4th 2008 to October 1st 2012. The bin size is 45 day. The background diffuse emission (both galactic and extragalactic) is fixed to the best-fit parameters obtained for the overall time fit. While some variability may be present, limited statistics do not yet allow to make definite conclusions.

Interestingly however, a similar test for the light curve with 45 day bins gives in $\chi^2/d.o.f. \approx 1.61$ and $P(\chi^2) = 0.015$, indicating a possible variability on 45-day time scale. Unfortunately, because of limited statistics, we cannot make a definite conclusion in this regard. The light curve with 45 day bins is shown in Figure 5.2, with the dot-dashed line indicating the flux from the source for the whole time period (result of likelihood analysis).
In addition, the variability of observed flux above and below 4 GeV is performed. Low detection significance of the component above 4 GeV (TS=124.4) does not allow us to investigate possible variability timescale, whereas for the other component search of variability is performed for 15, 30, 45 and 60 day bins under the same screening conditions described above. So significant variability have been found in any time scale, however still the hints for the variability are present in the lightcurve of 45 day bins $\chi^2/d.o.f. = 1.75$.

5.4 Discussion and Conclusion-1

In the case of high-frequency-peaked BL Lac objects, homogeneous leptonic synchrotron-self-Compton (SSC) jet models often provide reasonable descriptions of their overall spectral energy distributions (SEDs). For Cen A, however, classical one-zone SSC models (under the proviso of modest Doppler

beaming) are unable to satisfactorily account for its core SED up to the highest energies [cf. 17, 37, 7]. It seems thus well possible, that an additional component contributes to the observed emission at these energies [e.g., 37, 47]. The results presented here indeed provides support for such a consideration. Our analysis of the 4 yr-data set reveals that the HE core spectrum of Cen A

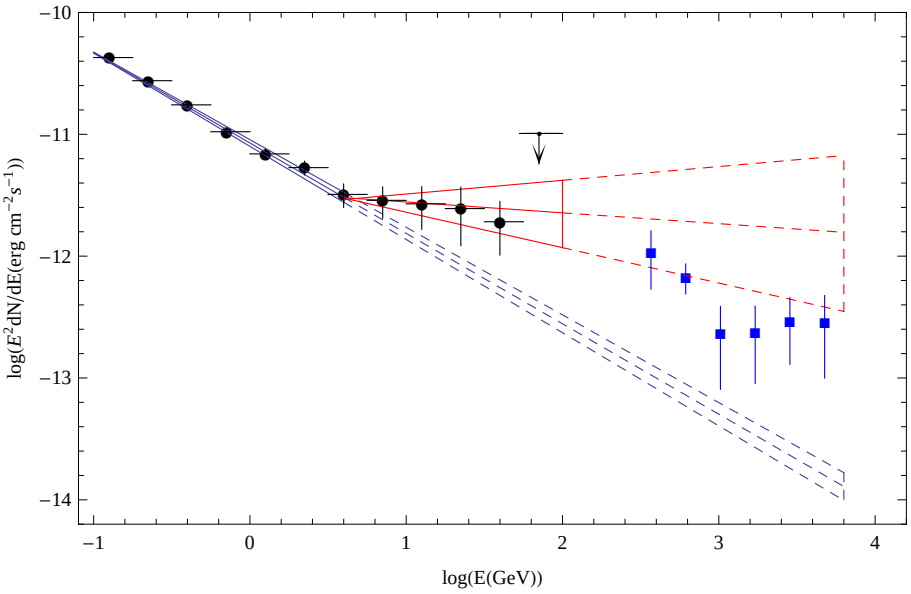

Figure 5.3: Gamma-ray spectrum for the core of Cen A from high (*Fermi* , this work) to very high (H.E.S.S., blue squares) energies. The blue bowtie represents a power-law with photon index 2.74, and the red bowtie a power-law with photon index 2.09. The dashed lines show extrapolations of these models to higher energies. The power-law extrapolation of the low-energy component (blue lines) would under-predict the fluxes observed at TeV energies.

shows a "break" with photon index changing from $\simeq 2.7$ to $\simeq 2.1$ at an energy of $E_b \simeq 4$ GeV. This break is unusual in that the spectrum gets harder instead of softer, while typically the opposite occurs. For a distance of 3.8 Mpc, the detected photon flux $F_\gamma = (1.68 \pm 0.04) \times 10^{-7}$ photon cm^{-2}s^{-1} for the component below 4 GeV corresponds to an apparent (isotropic) γ-ray luminosity of $L_\gamma(0.1 - 4\ \mathrm{GeV}) \simeq 10^{41}$ erg s^{-1}. The component above 4 GeV, on the other hand, is characterized by an isotropic HE luminosity of $L_\gamma(> 4\mathrm{GeV}) \simeq 1.4 \times 10^{40}$ erg s^{-1}. This is an order of magnitude less when

compared with the first component, but still larger than the VHE luminosity reported by H.E.S.S. $L_\gamma(> 250\,\mathrm{GeV}) = 2.6 \times 10^{39}\,\mathrm{erg\,s^{-1}}$ [9]. All luminosities are below the Eddington luminosity corresponding to the black hole mass in Cen A; nevertheless, they are still quite impressive when compared with the other nearby radio galaxy M87 containing a much more massive black hole.

Figure 5.3 shows the gamma-ray spectrum for the core of Cen A up to TeV energies. As one can see, the flux expected based on a power-law extrapolation of the low-energy component (below the break) clearly falls below the TeV flux reported by H.E.S.S.. Although the uncertainties in the photon index are large, it is clear that the spectrum becomes harder above 4 GeV. Remarkably, a simple extrapolation of the second (above the break) high-energy component to TeV energies could potentially allow one to match the average H.E.S.S. spectrum. These spectral considerations support the conclusion that we may actually be dealing with two (or perhaps even more) components contributing to the HE gamma-ray core spectrum of Cen A. Our analysis of the HE light curves provides some weak indication for a possible variability on 45 day time scale, but the statistics are not sufficient to draw clear inferences.

The limited angular resolution ($\sim$ 5 kpc) and the lack of significant variability introduces substantial uncertainties as to the production site of the HE gamma-ray emission. In principle, the hard HE component could originate from both a very compact (sub-pc) and/or extended (multi-kpc) region(s). The double-peaked nuclear SED of Cen A has been reasonably well-modeled up to a few GeV in terms of SSC processes occurring in its inner jet [e.g., 17, 7]. In this context, the hardening on the HE spectrum above 4 GeV would indeed mark the appearance of a physically different component. This additional component could in principle be related to a number of different (not mutually exclusive) scenarios, such as (i) non-thermal processes in its black hole magnetosphere [47], (ii) multiple SSC-emitting components (i.e., differential beaming)[37] or (iii) photo-meson interactions of protons in the inner jet [35, 49], (iv) γ-ray induced pair-cascades in a torus-like region (at $\sim 10^3 r_s$) [e.g. 48] (v) secondary Compton up-scattering of host galaxy starlight [51] or (vi) inverse-Compton (IC) processes in the kpc-scale jet [e.g. 29]. What concerns the more compact scenarios (i)-(iv) just mentioned: Opacity considerations do not a priori exclude a near-BH-origin, but could potentially affect the spectrum towards highest energies [e.g. 46]. A SSC multi-blob VHE contribution, on the other hand, requires the soft gamma-rays to be due to synchrotron instead of IC processes, in which case correlated variability might

be expected. Photo-meson ($p\gamma$) interactions with, e.g., UV or IR background photons (n_γ) require the presence of UHECR protons, which seems feasible for Cen A. However, as the mean free paths $\lambda \sim 1/(\sigma_{p\gamma} n_\gamma K_p)$ of protons through the relevant photon fields are comparatively large, usually only a modest fraction of the proton energy can be converted into secondary particles. Models of this type thus tend to need an injection power in high-energy protons exceeding the average jet power of $\sim 10^{43-44}$ erg/s [e.g. 57]. The efficiency of IC-supported pair cascades in Cen A, on the other hand, appears constrained by low accretion modes and the possible absence of a dust torus. Considering the more extended scenarios (v)-(vi): Partial absorption ($\sim 1\%$) of nuclear gamma-rays by starlight in the inner part of the host galaxy, and subsequent up-scattering of starlight photons could potentially introduce another HE contribution. However, the efficiency for this process is low, so that a high VHE injection power into the ambient medium is required, and the predicted spectral shape does not seem to match well. Compton-upscattering of starlight photon by energetic electrons in the kpc-scale jet also seems to have difficulties in reproducing the noted HE characteristics.

Finally, let us mention that gamma-ray production may perhaps also be related to relativistic protons interacting with the ambient gas in the large (kpc) scale regions, e.g., the overall elliptical galaxy NGC 5128 or the densest part of its dust lane. Note that the γ-ray luminosity $\approx 10^{41}$ erg/s above 100 MeV is larger by two orders of magnitude than the γ-ray luminosity of the Milky Way, which could be related to a higher rate of cosmic-ray production and a more effective confinement in the case of NGC 5128. Moreover, gamma-rays might also be produced in a diluted $R_{\rm halo} \sim 30$ kpc (halo) region of this galaxy. Despite the low density of gas, gamma-ray production on characteristic timescale $t_{\rm pp} \approx 3 \times 10^9 (n/10^{-2}{\rm cm}^{-3})^{-1}$ yr can be effective, even for a relatively fast diffusion of cosmic rays in this region. More specifically, the efficiency could be close to one, if the diffusion coefficient at multi-GeV energies does not exceed $D \sim R_{\rm halo}^2/t_{\rm pp} \sim 10^{29}$ cm^2/s. This seems an interesting possibility, especially for the second (hard) HE component with photon index close to 2.1, in the context of its similarity to the gamma-ray spectrum of the so-called 'Fermi Bubbles' around the center of our Galaxy [53]. The much higher luminosity (by $\sim 2-3$ orders of magnitude) of the second component compared to the gamma-ray luminosity of the Fermi Bubbles seems quite natural, given the much larger energy available in Cen A, in particular in the form of kinetic energy of its jet.

The results presented here provide observational evidence for an addi-

tional contribution at the highest energies and a more complex spectral gamma-ray behavior than previously anticipated. While considerations like those mentioned above may lead one to favor one production scenario over the other, none of them cannot be easily discarded. In fact, it is well conceivable that several of them contribute to the observed gamma-ray emission. Definite progress in this regard could be achieved in case of a significant detection of gamma-ray time variability.

5.5 The lobes of Cen A

The data used for the study of γ-ray emission from the lobes of CenA are from the beginning of the operation until November 14, 2011, amounting to ~ 3 yr of data (MET 239557417– 342956687). We used the standard LAT analysis software (v9r23p1)[2]. To avoid systematic errors due to poor determination of the effective area at low energies, we selected only events with energies above 200 MeV. The region-of-interest (ROI) was selected to be a rectangular region of size $14^\circ \times 14^\circ$ centered on the position of Cen A (RA $= 201^\circ 21' 54''$, DEC $= -43^\circ 1' 9''$). To reduce the effect of Earth albedo backgrounds, time intervals when the Earth was appreciably in the FoV (specifically, when the center of the FoV was more than 52° from zenith) as well as time intervals when parts of the ROI were observed at zenith angles $> 105^\circ$ were also excluded from the analysis. The spectral analysis was performed based on the P7v6 version of the post-launch instrument response functions (IRFs). We modeled the Galactic background component using the LAT standard diffuse background model *gal_2yearp7v6_v0* and we left the overall normalization and index as free parameters. We also used *iso_p7v6source* as the isotropic γ-ray background.
The resulting Fermi-LAT counts map for the 3 yr data set is shown in Figure 5.4(a). The (green) crosses show the position of the point-like sources from the 2FGL catalog ([43]) within the ROI. Extended emission to the north and south of Cen A is detected with significances of TS > 100 ($10\,\sigma$) and TS > 400 ($20\,\sigma$), respectively.

[2]http://fermi.gsfc.nasa.gov/ssc

5.5.1 Spatial analysis

Events with energies between 200 MeV and 30 GeV were selected. The residual image after subtracting the diffuse background and point-like sources including the core of Cen A is shown in Figure 5.4(b). The fluxes and spectral indices of 11 other point-like sources generated from the 2FGL catalog within the ROI are also left as free parameters in the analysis. The 2FGL catalog source positions are shown in Figure 5.4(a), where 2FGL J1324.0-4330e accounts for the lobes (both north and south). A new point-like source (2FGL J1335.3-4058), located at RA $= 203°49'30'', \mathrm{DEC} = -40°34'48''$ accounts for some residual emission from the north lobe, although no known source at other wavelengths is found to be associated. We treat it as part of the north lobe here. The core of Cen A is modeled as a point-like source. Then the following steps were performed:

(1) To evaluate the total (extended) HE γ-ray emission we first used a template based on the residual map (T1; corresponding to the blue contours in Figure 5.5). The TS values for the south and the north lobe in this template are 411 and 155, respectively. The residual map was also compared with radio (WMAP, 22 GHz) lobe contours (green contours overlaid on Figure 5.4(b)). While lower-frequency radio maps exist, we expect the higher-frequency 22 GHz map to better represent the GeV-emitting particles. We find that the south lobe of the HE γ-ray image is similar to the south lobe of the radio one, whereas the HE emission in the north extends beyond the radio lobe emission region.
(2) To understand this feature better, we re-fitted the excess using an additional template (T2; red contours in Figure 5.6) generated from the radio (WMAP) image. The two templates are shown in Figure 5.5, and the corresponding residual maps are shown in Figure 5.4. While there is some residual emission to the north of Cen A for template T2, this residual emission is obviously absent from template T1. The qualitative features of the different residual maps are confirmed by the corresponding TS values, which are listed in Table 5.1. Accordingly, the HE south lobe seems to agree reasonably well with the radio south lobe, whereas for the north lobe, the template generated from the radio lobe (T2) fits the HE excess substantially worse than T1 (110 vs 155).

(3) To further investigate a possible extension (or contribution of a background source) of the north lobe, we evaluated the projection of a rectangular

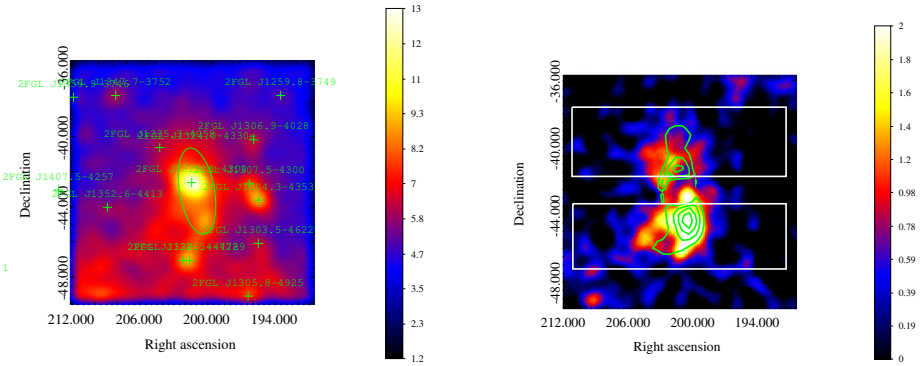

(a) LAT counts map of the 14° × 14° ROI. **(b)** Excess map after background subtraction.

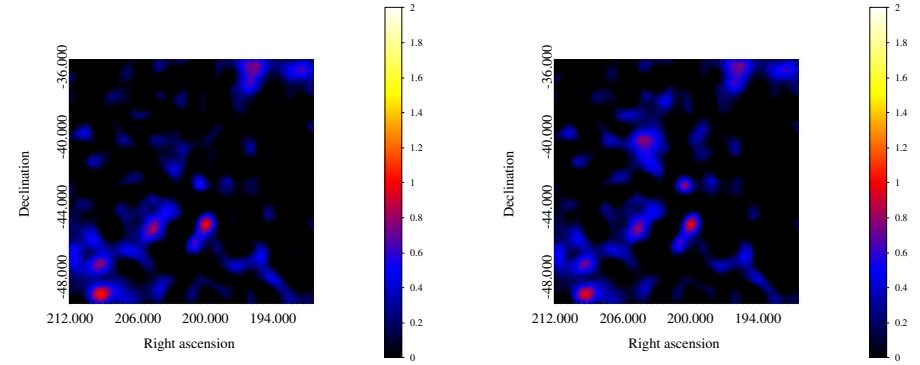

(c) Residual map for template T1. **(d)** Residual map for template T2.

Figure 5.4: The different maps for the Cen A region: (a) LAT counts map of the 14° × 14° region of interest (ROI) around the position of Cen A. The counts map is smoothed with a Gaussian of kernel 0.8°. The green crosses mark the position of the 2FGL point-like sources. (b) Excess map after subtraction of diffuse background, point-like sources and Cen A core. The contours are WMAP radio lobe contours, while the white boxes represent the projection regions discussed in Sec. 5.5.1. (c) Residual map using template T1 for the lobes. (d) Residual map using the radio template T2 for the lobes.

Table 5.1: TS value for the two templates used.

Model	north Lobe	south Lobe
T1	155	411
T2	110	406

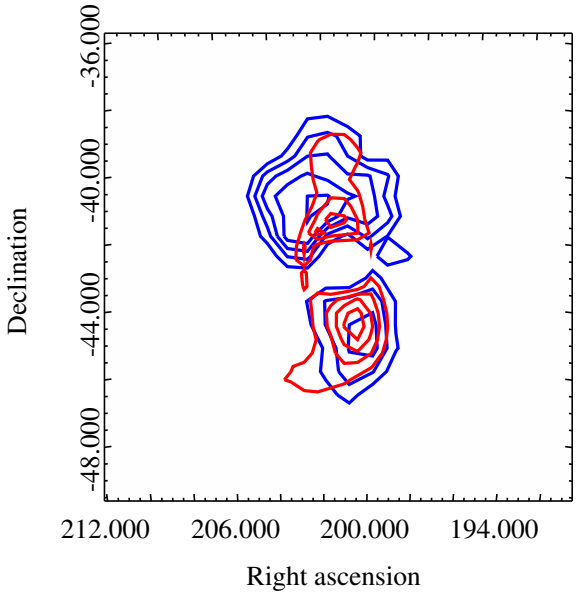

Figure 5.5: Two templates used in the analysis. The blue contours correspond to T1 and the red to T2.

region on the excess image (in white in Figure 5.4(b)). Figure 5.6 shows the projection for the north and south regions for Fermi-LAT image (in black) and the radio one (in red). The south projection for the radio map is well-fitted by a single Gaussian centered at ~ 0.05 (0 is defined as the center of the rectangle on $RA = 201°21'54'', DEC = -43°1'9''$) with an extension of $\sigma = 0.99°$. For the Fermi-LAT map the Gaussian is centered at ~ 0.5 and has $\sigma = 1.01°$, compatible with the radio map projection. In contrast, the north projection for the Fermi-LAT map has a Gaussian profile with $\sigma = 1.68°$, while for the radio map σ is 0.97°. The extension in the north projections for the Fermi-LAT map indicates that the γ-ray north lobe is more extended than the radio one or that an (otherwise unknown) source in the background may be contributing to the total emission.

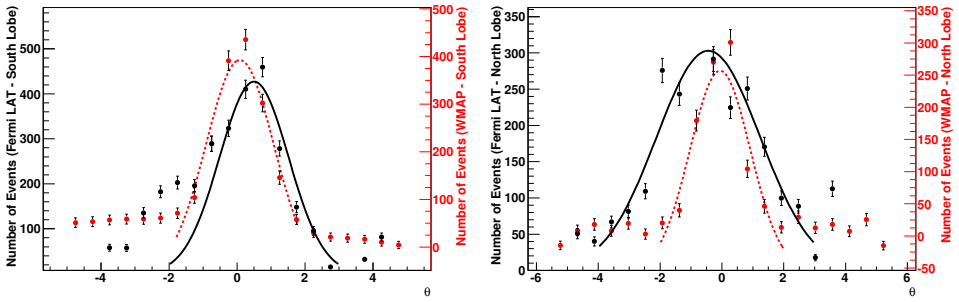

(a) Projection of the south lobe **(b)** Projection of the north lobe

Figure 5.6: Projection of the rectangular region shown in Figure 5.4(b) for both lobes. The curves are Gaussian fits, with WMAP data in red and Fermi-LAT data in black. Units for the positional (x) axis are degrees.

5.5.2 Spectral analysis

Our morphological analysis indicates some incongruity between the morphology of the radio lobe and γ-ray lobe in the north. Hence, to model the γ-ray lobe as self-consistently as possible, we used the template generated with the residual map (T1). Integrating the whole γ-ray emission observed, we then derived the total flux and index in the 100 MeV to 30 GeV energy range. For the north lobe the integral HE flux is $(0.93 \pm 0.09) \times 10^{-7}$ph cm^{-2}s^{-1} and the photon index is 2.24 ± 0.08, while for the south lobe we find $(1.4 \pm 0.2) \times 10^{-7}$ph cm^{-2}s^{-1} and 2.57 ± 0.07, respectively. The results are summarized in Table 5.2, where the subscripts 3a and 10m refer to the three-year data (analyzed here) and the ten-month data (reported in [4]), respectively. We find that the flux and photon indices in the T2 templates are similar to the ten-month data. On the other hand, the analysis using the T1 template results in a harder spectrum for the north lobe.

To derive the spectral energy distribution (SED) we divided the energy range into logarithmically spaced bands and applied *gtlike* in each of these bands. Only the energy bins for which a signal was detected with a significance of at least 2σ were considered, while an upper limit was calculated for those below. As a result, there are seven bins in the SED for the south lobe.

To clarify the origin of the γ-ray emission, we evaluated the spectrum in different parts of each lobe. To this end, we divided each lobe into two parts and used *gtlike* to evaluate the spectrum. In the south lobe the resulting photon

index is 2.8 ± 0.2 near the Cen A core and 2.3 ± 0.1 far away from the core. Unfortunately, the statistics are still not high enough to claim a clear hardening of the spectrum. For the northern lobe, both parts appear to be consistent with values of 2.2 ± 0.2.

Table 5.2: Fluxes and spectra of the lobes

Source Name	Φ_{3a}(T1)	Γ_{3a}(T1)	Φ_{10m}	Γ_{10m}	Φ_{3a}(T2)	Γ_{3a}(T2)
South Lobe	1.43 ± 0.15	2.57 ± 0.07	1.09 ± 0.24	2.60 ± 0.15	1.40 ± 0.15	2.56 ± 0.08
North Lobe	0.93 ± 0.09	2.24 ± 0.08	0.77 ± 0.20	2.52 ± 0.16	0.64 ± 0.15	2.56 ± 0.08

Φ is the integral flux (100 MeV to 30 GeV) in units of $10^{-7}\mathrm{ph} \cdot \mathrm{cm}^{-2}\mathrm{s}^{-1}$ and Γ is the photon index. The subscripts "3a" and "10m" refer to the three-year data analyzed here and to the ten-month results (based on a WMAP template) reported in [4], respectively.

5.6 The origin of the non-thermal lobe emission

Using the WMAP and Fermi-LAT results reported here, we can characterize the spectral energy distributions for the north and the south lobe. While the radio emission is usually taken to be caused by electron synchrotron emission, the origin of the HE γ-ray emission could in principle be related to both leptonic (inverse-Compton scattering) and hadronic (e.g., pp-interaction) processes. In the following we discuss possible constraints for the underlying radiation mechanism as imposed by the observed SEDs.

5.6.1 Inverse-Compton origin of γ-rays

Both the HE γ-ray and the radio emission could be accounted for in a leptonic scenario. In the simplest version, a single population of electrons $N(\gamma, t)$ is used to model the SED through synchrotron and inverse-Compton emission, with particle acceleration being implicitly treated by an effective injection term $Q = Q(\gamma, t)$. The latter allows us to distinguish acceleration caused by, e.g., multiple shocks or stochastic processes (e.g., [44]) from emission, and enables a straightforward interpretation. The kinetic equation describing the

energetic and temporal evolution of the radiating electrons can then be written as

$$\frac{\partial N}{\partial t} = \frac{\partial}{\partial \gamma}\left(P\,N\right) - \frac{N}{\tau_{esc}} + Q\,, \tag{5.6.1}$$

where $P = P(\gamma) = -\frac{d\gamma}{dt}$ is the (time-independent) energy loss rate and $\tau_{\rm esc}$ is the characteristic escape time. For negligible escape (as appropriate here, given the large size of the γ-ray emitting region) and quasi continuous injection (considered as a suitable first-order approximation given the short lifetime of TeV electrons and the scales of the lobes) $Q(\gamma, t) = Q(\gamma)$, the solution of the kinetic equation becomes

$$N(\gamma, t) = \frac{1}{P(\gamma)} \int_{\gamma}^{\gamma_0} Q(\gamma) d\gamma\,, \tag{5.6.2}$$

where γ_0 is found by solving the characteristic equation for a given epoch t, $t = \int_{\gamma}^{\gamma_0} \frac{d\gamma}{P(\gamma)}$ (e.g., [12]). If synchrotron or inverse-Compton (Thomson) losses ($P(\gamma) = a\,\gamma^2$) provide the dominant loss channel, then $\gamma_0 = \gamma/(1 - a\gamma t)$, so that at the energy $\gamma_{\rm br} = \frac{1}{a\,t}$ the stationary power-law electron injection spectrum steepens by a factor of 1 (cooling break) due to radiative losses, naturally generating a broken power-law.
We used the above particle distribution described in eq. (5.6.2) for a representation of the observed lobe SEDs. The magnetic field strength B, the maximum electron energy $\gamma_{\rm max}$ and the epoch time t were left as free parameters to model the data. Klein-Nishina (KN) effects on the inverse-Compton-scattered HE spectrum were taken into account (following [10]).
Figure 5.7 shows the SED results obtained for the north and south lobes. The HE part of both spectra can be described by a power-law with photon index $\Gamma_\gamma \simeq 2.2$ and 2.6 for the north and the south lobe, respectively. At low energies, the south lobe spectrum shows a synchrotron peak at about 5 GHz, while the north lobe is well described by a power-law with an index > 2. Note that if one would use a simple power-law electron injection spectrum $Q(\gamma) \propto \gamma^{-\alpha}$, evolving in time with a cooling break, to describe the HE γ-ray spectrum, a power index $\alpha = 3.2$ would be required for the south lobe. Yet, assuming that the same electron population is responsible for both the radio-synchrotron and HE inverse-Compton emission, such a value would be in conflict with the results obtained from the WMAP data analysis, indicating an electron population with power-law index $\alpha \simeq 2$ based on the

detected synchrotron emission. As it turns out, however, this problem could be accommodated by considering a more natural spectral input shape, e.g., an electron injection spectrum with an exponential cut-off

$$Q(\gamma) = Q_0 \, \gamma^{-\alpha} \exp\left(-\frac{\gamma}{\gamma_{\rm max}}\right) , \tag{5.6.3}$$

where the constant Q_0 can be obtained from the normalization to the injection power $L = m_e c^2 \int Q(\gamma) \, \gamma \, d\gamma$.
The age of the giant lobe emission, and associated with this, the duration of particle acceleration activity, is somewhat uncertain. Dynamical arguments suggest a lower limit $> 10^7$ yr for the giant radio lobes, while synchrotron spectral aging arguments indicate an age $\lesssim 3 \times 10^7$ yr (e.g., [34, 11, 28]). The observed GeV extension in itself would already imply an extreme lower limit of $R/c > 10^6$ yr. In the following we therefore discuss the SED implications for an epoch time t between 10^7 yr and 10^8 yr. As it turns out, the modeling of the GeV data provides support for a maximum lobe age of $\sim 8 \times 10^7$ yr.
For the south lobe, the radio data suggest a break frequency $\nu_{\rm br} = 5$ GHz above which the spectrum drops abruptly. The break in the synchrotron spectrum is related to the break in the electron spectrum via $\nu_{\rm br} = 1.3 \, \gamma_{\rm br}^2 \, B_{1\mu G}$ Hz. In principle, a change in the spectral shape of the electron population might be caused by cooling effects or/and the existence of a maximum energy for the electron population. For a minimum epoch time $t_{\rm min} = 10^7$ yr, cooling would affect the synchrotron spectrum at frequency $\approx 80 B_{1\mu G}$ GHz, much higher than inferred from the radio data. Therefore, to obtain a break at 5 GHz in the south lobe, a maximum energy in the electron population ($\gamma_{\rm max}$), lower than $\gamma_{\rm br}$ defined by $t = t_{\rm min}$ would be needed. On the other hand, for a maximum epoch time $t_{\rm max} = 8 \times 10^7$ yr, the power-law spectral index changes at frequency $\simeq 1 B_{1\mu G}$ GHz, providing a satisfactory agreement with the radio data. In this case the maximum electron energy is obtained from the radio data above the break frequency 5 GHz. Results for the considered minimum and maximum epoch time, and for a fixed power-law electron index $\alpha = 2$ are illustrated in Figures 5.7 and 5.8. Note that for $B \leq 3\mu$G, the energy loss rate $P(\gamma)$ is dominated by the IC channel only, so that the results of the calculations are quite robust.
Figure 5.7 shows a representation of the SED for the north and the south lobe, respectively, using the parameters $t_{\rm min} = 10^7$ yr and $\gamma_{\rm max} = 1.5 \times 10^5$. The dashed line shows the HE contribution produced by inverse-Compton

scattering of cosmic microwave background photons by relativistic electrons within the lobes. In this case the resulting γ-ray flux can only describe the first two data points and then drops rapidly. Consequently, to be able to account for the observed HE spectrum, extragalactic background light photons need to be included in addition to CMB photons (see dot-dashed line in Figure 5.7). Upscattering of infrared-to-optical EBL photons was already required in the stationary leptonic model reported in the original Fermi paper ([4]). In our approach we adopt the model by [22] to evaluate this EBL contribution. The solid line in Figure 5.7 represents the total (CMB+EBL) inverse-Compton contribution. The maximum total energy of electrons in both lobes is found to be $\sim 2 \times 10^{58}$ erg and the energy in the magnetic fields is roughly 25% of this. Dividing the total energy by the epoch time 10^7 yr would imply a mean kinetic power of the jets inflating the lobes of $\simeq 7 \times 10^{43}$ erg/s, roughly two orders of magnitude lower than the Eddington power inferred for the black hole mass in Cen A, yet somewhat above the estimated power of the kpc-scale jet in the current epoch of jet activity ([18]). This could indicate that the jet was more powerful in the past. Obviously, the requirement on the mean jet power can be significantly reduced if one assumes an older age of the lobes. Figure 5.8 shows a representation of the SED for an epoch time $t_{\rm max} = 8 \times 10^7$ yr, with a maximum electron Lorentz factor $\gamma_{\rm max} = 2.5 \times 10^6$ and 1.5×10^6 for the north lobe and the south lobe, respectively. Note that in this case the contribution by inverse-Compton scattering of CMB photons alone is sufficient to account for the observed HE spectrum (see the solid line in Figure 5.8). The inverse-Compton contribution of EBL photons only becomes important at higher energies (see the dot-dashed line in Figure 5.8). On the other hand, for an epoch time t exceeding $t_{\rm max} = 8 \times 10^7$ yr, the high-energy part of the SED would no longer be consistent with the data (see the dashed line in Figure 5.8 for $t = 10^8$ yr). This could be interpreted as additional evidence for a finite age $< 10^8$ yr of the lobes. The maximum total energy of electrons in both lobes is found to be $\approx 6 \times 10^{57}$ erg, with the total energy in particles and fields comparable to the 10^7yr-case, thus requiring only a relatively modest mean kinetic jet power of $\sim 10^{43}$ erg/s.

5.6.2 Hadronic γ-rays?

Once protons are efficiently injected, they are likely to remain energetic since the cooling time for pp-interactions is $t_{\rm pp} \approx 10^{15}(n/1\ cm^{-3})^{-1}$ s. High-

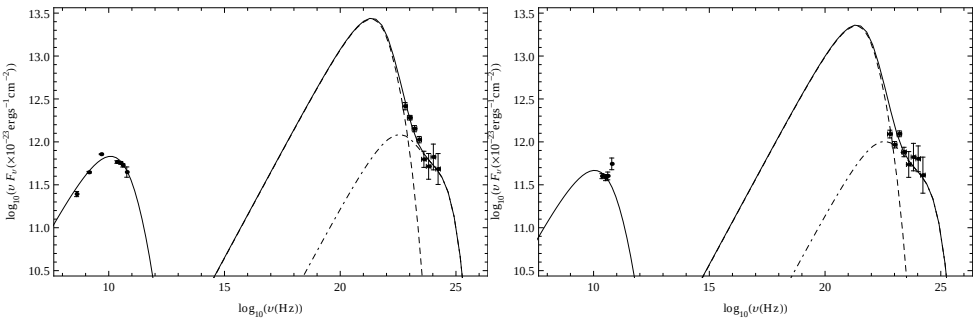

(a) South lobe **(b)** γ-ray excess (lobe) region in the north

Figure 5.7: Synchrotron and inverse-Compton fluxes for $t = 10^7$ yr. The radio data for the south lobe are from [28] (sum of region 4 and region 5 in their Table 1), while the radio data for the north region are from the WMAP analysis in this paper. The mean magnetic field value B used for the north and the south lobe is 0.39 μG and 0.43 μG, respectively. The dot-dashed line refers to the IC contribution due to EBL upscattering.

energy protons interacting with the ambient low-density plasma can then produce daughter mesons and the π^0 component decays into two γ-rays. The data reported here allow us to derive an upper limit on the energetic protons contained in the lobes of Cen A. As before, we use a power-law proton distribution with an exponential cut-off, i.e.,

$$N(\gamma_p) = N_0 \, \gamma_p^{-\alpha} \exp\left(-\frac{\gamma_p}{\gamma_{\mathrm{max}}}\right)$$

where the constant N_0 can be expressed in terms of the total proton energy $W_p = m_p c^2 \int \gamma_p \; N(\gamma_p) \, d\gamma_p$. Current estimates for the thermal plasma density in the giant radio lobes of Cen A suggest a value in the range $n \simeq (10^{-5} - 10^{-4})$ cm^{-3} (e.g., [33, 21]). We used $n = 10^{-4}$ cm^{-3} for the model representation shown in dotted line in Figure 5.8. In both lobes, the power-law index of the proton population is $\alpha = 2.1$, and the high-energy cut-off is $E_{\mathrm{max}} \simeq 55$ GeV. The maximum total energy W_p is proportional to the gas number density n, so that $W_p \simeq 10^{61} (n/10^{-4} \; \mathrm{cm}^{-3})^{-1}$ erg, obtained here, should be considered as an upper limit. In principle, protons could be accumulated over the whole evolutionary timescale of the lobes. For a long timescale of $\geq 10^9$ yr, an average injection power $\leq 3 \times 10^{44}$ erg/s and a

mean cosmic-ray diffusion coefficient of $D \sim R^2/t \lesssim 3 \times 10^{30}(R/100\ \mathrm{kpc})^2$ cm^2/s would be needed.

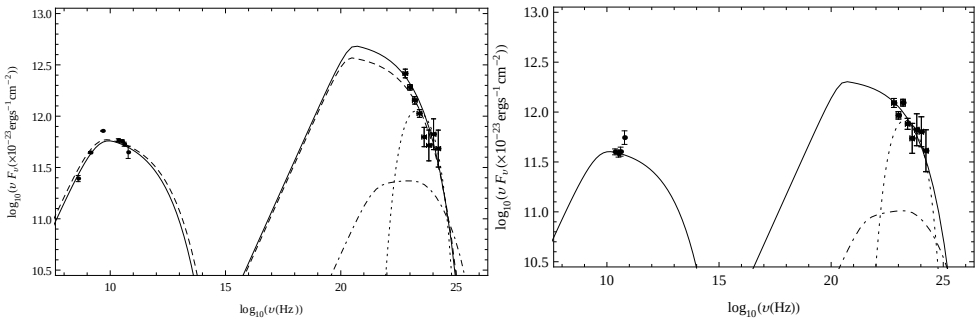

(a) South lobe **(b)** γ-ray excess (lobe) region in the north

Figure 5.8: Synchrotron and inverse-Compton fluxes for $t = 8 \times 10^7$ yr. The mean magnetic field value B for the south lobe and the γ-ray excess region in the north lobe is 0.91 μG and 1.17 μG, respectively. The dot-dashed line refers to the IC contribution due to EBL upscattering. The dashed line (a) shows the result for $t = 10^8$ yr. The possible γ-ray flux expected from pp-interactions for a thermal gas density $n = 10^{-4}\ cm^{-3}$ are also shown (dotted line).

5.7 Discussion and conclusion-2

Results based on an detailed analysis of 3 yr of Fermi-LAT data on the giant radio lobes of Cen A shows that they are detected with a significance more than twice as high as reported before (i.e., with more than 10 and 20σ for the northern and the southern lobe, respectively) which allows a better determination of their spectral features and morphology. A comparison of the Fermi-LAT data with WMAP data indicates that the HE γ-ray emission regions do not fully coincide with the radio lobes. There is of course no a priori reason for them to coincide. The results reported here particularly support a substantial HE γ-ray extension beyond the WMAP radio image for the northern lobe of Cen A. We have reconstructed the SED based on data from the same emission region. A satisfactory representation is possible in a time-dependent leptonic scenario with radiative cooling taken into account self-consistently and injection described by a single power-law with exponential cut-off. The results imply a finite age $< 10^8$ yr of the lobes and a

mean magnetic field strength $B \lesssim 1\mu$G. While for lobe lifetimes on the order of 8×10^7 yr, inverse-Compton up-scattering of CMB photons alone would be sufficient to account for the observed HE spectrum, up-scattering of EBL photons is needed for shorter lobe lifetimes. In a leptonic framework, the HE emission directly traces (via inverse-Compton scattering) the underlying relativistic electron distribution and thereby provides a spatial diagnostic tool. The radio emission, arising from synchrotron radiation, on the other hand also traces the magnetic field distribution. Together, the HE γ-ray and the radio emission thus offer important insights into the physical conditions of the source. That the HE emission seems extended beyond the radio image could then be interpreted as caused by a change in the magnetic field characterizing the region. This would imply that our quasi-homogeneous SED model for the HE lobes can only serve as a first-order approximation and that more detailed scenarios need to be constructed to fully describe the data. This also applies to the need of incorporating electron re-acceleration self-consistently. Extended HE emission could in principle also be related to a contribution from hadronic processes. The cooling timescales for protons appear much more favorable. On the other hand, both the spectral shape of the lobes and the required energetics seem to disfavor pp-interaction processes as sole contributor.

Bibliography

[1] A. A. Abdo, M. Ackermann, M. Ajello, , and et al.
Fermi Large Area Telescope Gamma-Ray Detection of the Radio Galaxy M87.
ApJ, 707:55–60, December 2009.

[2] A. A. Abdo, M. Ackermann, M. Ajello, and et al.
Fermi Discovery of Gamma-ray Emission from NGC 1275.
ApJ, 699:31–39, July 2009.

[3] A. A. Abdo, M. Ackermann, M. Ajello, and et al.
Fermi Gamma-Ray Imaging of a Radio Galaxy.
Science, 328:725–, May 2010.

[4] A. A. Abdo, M. Ackermann, M. Ajello, et al.
Fermi Gamma-Ray Imaging of a Radio Galaxy.
Science, 328:725–, May 2010.

[5] A. A. Abdo, M. Ackermann, M. Ajello, and et al.
Fermi Large Area Telescope Observations of Misaligned Active Galactic Nuclei.
ApJ, 720:912–922, September 2010.

[6] A. A. Abdo, M. Ackermann, M. Ajello, and et al.
Fermi Large Area Telescope View of the Core of the Radio Galaxy Centaurus A.
ApJ, 719:1433–1444, August 2010.

[7] A. A. Abdo, M. Ackermann, M. Ajello, et al.
Fermi Large Area Telescope View of the Core of the Radio Galaxy Centaurus A.
ApJ, 719:1433–1444, August 2010.

[8] F. A. Aharonian.
Proton-synchrotron radiation of large-scale jets in active galactic nuclei.
MNRAS, 332:215–230, May 2002.

[9] **F. Aharonian**, A. G. Akhperjanian, G. Anton, et al.
Discovery of Very High Energy γ-Ray Emission from Centaurus a with H.E.S.S.
ApJL, 695:L40–L44, April 2009.

[10] **F. Aharonian** and A. M. Atoyan.
Compton scattering of relativistic electrons in compact X-ray sources.
Ap&SS, 79:321–336, October 1981.

[11] H. Alvarez, J. Aparici, J. May, and P. Reich.
The radio continuum spectrum of Centaurus A's large-scale components.
A&A, 355:863–872, March 2000.

[12] A. M. Atoyan and **F. Aharonian**.
Modelling of the non-thermal flares in the Galactic microquasar GRS 1915+105.
MNRAS, 302:253–276, January 1999.

[13] W. B. Atwood, A. A. Abdo, M. Ackermann, et al.
The Large Area Telescope on the Fermi Gamma-Ray Space Telescope Mission.
ApJ, 697:1071–1102, June 2009.

[14] S. D. Bloom and A. P. Marscher.
An Analysis of the Synchrotron Self-Compton Model for the Multi–Wave Band Spectra of Blazars.
ApJ, 461:657, April 1996.

[15] G. Bonnoli, G. Ghisellini, L. Foschini, F. Tavecchio, and G. Ghirlanda.
The γ-ray brightest days of the blazar 3C 454.3.
MNRAS, 410:368–380, January 2011.

[16] A. Celotti, L. Maraschi, and A. Treves.
A model for the spectral variability of BL Lacertae objects at high frequencies.
ApJ, 377:403–416, August 1991.

[17] M. Chiaberge, A. Capetti, and A. Celotti.
The BL Lac heart of Centaurus A.
MNRAS, 324:L33–L37, July 2001.

[18] J. H. Croston, R. P. Kraft, M. J. Hardcastle, et al.
High-energy particle acceleration at the radio-lobe shock of Centaurus A.
MNRAS, 395:1999–2012, June 2009.

[19] M. Eracleous and J. P. Halpern.
The ASCA X-Ray Spectrum of the Broad-line Radio Galaxy Pictor A: A Simple Power Law With No Fe Kα Line.
ApJ, 505:577–586, October 1998.

[20] B. L. Fanaroff and J. M. Riley.
The morphology of extragalactic radio sources of high and low luminosity.
MNRAS, 167:31P–36P, May 1974.

[21] I. J. Feain, R. D. Ekers, T. Murphy, et al.
Faraday Rotation Structure on Kiloparsec Scales in the Radio Lobes of Centaurus A.
ApJ, 707:114–125, December 2009.

[22] A. Franceschini, G. Rodighiero, and M. Vaccari.
Extragalactic optical-infrared background radiation, its time evolution and the cosmic photon-photon opacity.
A&A, 487:837–852, September 2008.

[23] G. Ghisellini, L. Maraschi, and A. Treves.
Inhomogeneous synchrotron-self-Compton models and the problem of relativistic beaming of BL Lac objects.
A&A, 146:204–212, May 1985.

[24] P. Giommi, G. Polenta, A. Lähteenmäki, and et al.
Simultaneous Planck, Swift, and Fermi observations of X-ray and γ-ray selected blazars.
A&A, 541:A160, May 2012.

[25] J.-L. Gómez, A. P. Marscher, and A. Alberdi.

86, 43, and 22 GHz VLBI Observations of 3C 120.
ApJL, 521:L29–L32, August 1999.

[26] J.-L. Gómez, A. P. Marscher, A. Alberdi, J. M. Martí, and J. M. Ibáñez.
Subparsec Polarimetric Radio Observations of 3C 120: A Close-up Look at Superluminal Motion.
ApJ, 499:221–226, May 1998.

[27] J. P. Halpern.
X-ray spectrum and variability of 3C 120.
ApJ, 290:130–135, March 1985.

[28] M. J. Hardcastle, C. C. Cheung, I. J. Feain, and Ł. Stawarz.
High-energy particle acceleration and production of ultra-high-energy cosmic rays in the giant lobes of Centaurus A.
MNRAS, 393:1041–1053, March 2009.

[29] M. J. Hardcastle and J. H. Croston.
Modelling TeV γ-ray emission from the kiloparsec-scale jets of Centaurus A and M87.
MNRAS, 415:133–142, July 2011.

[30] D. E. Harris, A. E. Mossman, and R. C. Walker.
The X-Ray Jet of 3C 120: Evidence for a Nonstandard Synchrotron Spectrum.
ApJ, 615:161–172, November 2004.

[31] R. C. Hartman, D. L. Bertsch, and S. D. Bloom.
The Third EGRET Catalog of High-Energy Gamma-Ray Sources.
ApJSS, 123:79–202, July 1999.

[32] D. C. Homan, R. Ojha, J. F. C. Wardle, D. H. Roberts, M. F. Aller, H. D. Aller, and P. A. Hughes.
Parsec-Scale Blazar Monitoring: Proper Motions.
ApJ, 549:840–861, March 2001.

[33] N. Isobe, K. Makishima, M. Tashiro, and H. Kaneda.
ASCA observations of the northern outer lobe edge of the radio galaxy Centaurus A.

In R. A. Laing and K. M. Blundell, editors, *Particles and Fields in Radio Galaxies Conference*, volume 250 of *Astronomical Society of the Pacific Conference Series*, page 394, 2001.

[34] F. P. Israel.
Centaurus A - NGC 5128.
A&AR, 8:237–278, 1998.

[35] M. Kachelrieß, S. Ostapchenko, and R. Tomàs.
TeV Gamma Rays from Ultrahigh Energy Cosmic Ray Interactions in the Cores of Active Galactic Nuclei: Lessons from Centaurus A.
PASA, 27:482–489, October 2010.

[36] J. Kataoka, Ł. Stawarz, Y. Takahashi, C. C. Cheung, M. Hayashida, P. Grandi, T. H. Burnett, A. Celotti, S. J. Fegan, P. Fortin, K. Maeda, T. Nakamori, G. B. Taylor, G. Tosti, S. W. Digel, W. McConville, J. Finke, and F. D'Ammando.
Broad-line Radio Galaxies Observed with Fermi-LAT: The Origin of the GeV γ-Ray Emission.
ApJ, 740:29, October 2011.

[37] J.-P. Lenain, C. Boisson, H. Sol, and K. Katarzyński.
A synchrotron self-Compton scenario for the very high energy γ-ray emission of the radiogalaxy M 87. Unifying the TeV emission of blazars and other AGNs?
A&A, 478:111–120, January 2008.

[38] Y. C. Lin, D. L. Bertsch, B. L. Dingus, C. E. Fichtel, R. C. Hartman, S. D. Hunter, G. Kanbach, D. A. Kniffen, J. R. Mattox, H. A. Mayer-Hasselwander, P. F. Michelson, C. von Montigny, P. L. Nolan, E. Schneid, P. Sreekumar, and D. J. Thompson.
EGRET Limits on High-Energy Gamma-Ray Emission from X-Ray– and Low-Energy Gamma-Ray–selected Seyfert Galaxies.
ApJL, 416:L53, October 1993.

[39] C. Ma, E. F. Arias, T. M. Eubanks, et al.
The International Celestial Reference Frame as Realized by Very Long Baseline Interferometry.
AJ, 116:516–546, July 1998.

[40] C. Ma, E. F. Arias, T. M. Eubanks, A. L. Fey, A.-M. Gontier, C. S. Jacobs, O. J. Sovers, B. A. Archinal, and P. Charlot.
The International Celestial Reference Frame as Realized by Very Long Baseline Interferometry.
AJ, 116:516–546, July 1998.

[41] A. P. Marscher, S. G. Jorstad, J.-L. Gómez, M. F. Aller, H. Teräsranta, M. L. Lister, and A. M. Stirling.
Observational evidence for the accretion-disk origin for a radio jet in an active galaxy.
Nature, 417:625–627, June 2002.

[42] E. Massaro, A. Tramacere, M. Perri, P. Giommi, and G. Tosti.
Log-parabolic spectra and particle acceleration in blazars. III. SSC emission in the TeV band from Mkn501.
A&A, 448:861–871, March 2006.

[43] P. L. Nolan, A. A. Abdo, M. Ackermann, M. Ajello, A. Allafort, E. Antolini, W. B. Atwood, M. Axelsson, L. Baldini, J. Ballet, and et al.
Fermi Large Area Telescope Second Source Catalog.
ApJSS, 199:31, April 2012.

[44] S. O'Sullivan, B. Reville, and A. M. Taylor.
Stochastic particle acceleration in the lobes of giant radio galaxies.
MNRAS, 400:248–257, November 2009.

[45] B. M. Peterson, L. Ferrarese, K. M. Gilbert, S. Kaspi, M. A. Malkan, D. Maoz, D. Merritt, H. Netzer, C. A. Onken, R. W. Pogge, M. Vestergaard, and A. Wandel.
Central Masses and Broad-Line Region Sizes of Active Galactic Nuclei. II. A Homogeneous Analysis of a Large Reverberation-Mapping Database.
ApJ, 613:682–699, October 2004.

[46] F. M. Rieger.
Nonthermal Processes in Black Hole-Jet Magnetospheres.
International Journal of Modern Physics D, 20:1547–1596, 2011.

[47] F. M. Rieger and **F. Aharonian**.
Centaurus A as TeV γ-ray and possible UHE cosmic-ray source.

A&A, 506:L41–L44, November 2009.

[48] P. Roustazadeh and M. Böttcher.
Very High Energy Gamma-ray-induced Pair Cascades in the Radiation Fields of Dust Tori of Active Galactic Nuclei: Application to Cen A.
ApJ, 728:134, February 2011.

[49] S. Sahu, B. Zhang, and N. Fraija.
Hadronic-origin TeV γ rays and ultrahigh energy cosmic rays from Centaurus A.
Phys. Rev. D, 85(4):043012, February 2012.

[50] P. Sreekumar, D. L. Bertsch, R. C. Hartman, P. L. Nolan, and D. J. Thompson.
GeV emission from the nearby radio galaxy Centaurus A.
Astroparticle Physics, 11:221–223, June 1999.

[51] Ł. Stawarz, **F. Aharonian**, S. Wagner, and M. Ostrowski.
Absorption of nuclear γ-rays on the starlight radiation in FR I sources: the case of Centaurus A.
MNRAS, 371:1705–1716, October 2006.

[52] H. Steinle, K. Bennett, H. Bloemen, W. Collmar, R. Diehl, W. Hermsen, G. G. Lichti, D. Morris, V. Schonfelder, A. W. Strong, and O. R. Williams.
COMPTEL observations of Centaurus A at MeV energies in the years 1991 to 1995.
A&A, 330:97–107, February 1998.

[53] M. Su, T. R. Slatyer, and D. P. Finkbeiner.
Giant Gamma-ray Bubbles from Fermi-LAT: Active Galactic Nucleus Activity or Bipolar Galactic Wind?
ApJ, 724:1044–1082, December 2010.

[54] A. Tramacere, P. Giommi, M. Perri, F. Verrecchia, and G. Tosti.
Swift observations of the very intense flaring activity of Mrk 421 during 2006. I. Phenomenological picture of electron acceleration and predictions for MeV/GeV emission.
A&A, 501:879–898, July 2009.

[55] A. Tramacere, E. Massaro, and A. M. Taylor.
Stochastic Acceleration and the Evolution of Spectral Distributions in Synchro-Self-Compton Sources: A Self-consistent Modeling of Blazars' Flares.
ApJ, 739:66, October 2011.

[56] R. C. Walker, J. M. Benson, and S. C. Unwin.
The radio morphology of 3C 120 on scales from 0.5 parsecs to 400 kiloparsecs.
ApJ, 316:546–572, May 1987.

[57] R.-Z. Yang, **N. Sahakyan**, E. de Ona Wilhelmi, **F. Aharonian**, and F. Rieger.
Deep observation of the giant radio lobes of Centaurus A with the Fermi Large Area Telescope.
A&A, 542:A19, June 2012.

[58] J. Zhang, J. M. Bai, L. Chen, and E. Liang.
X-Ray Radiation Mechanisms and Beaming Effect of Hot Spots and Knots in Active Galactic Nuclear Jets.
ApJ, 710:1017–1031, February 2010.